Volume 1
Number 3
May 2023
Pages 173–324

EES Catalysis

rsc.li/EESCatalysis

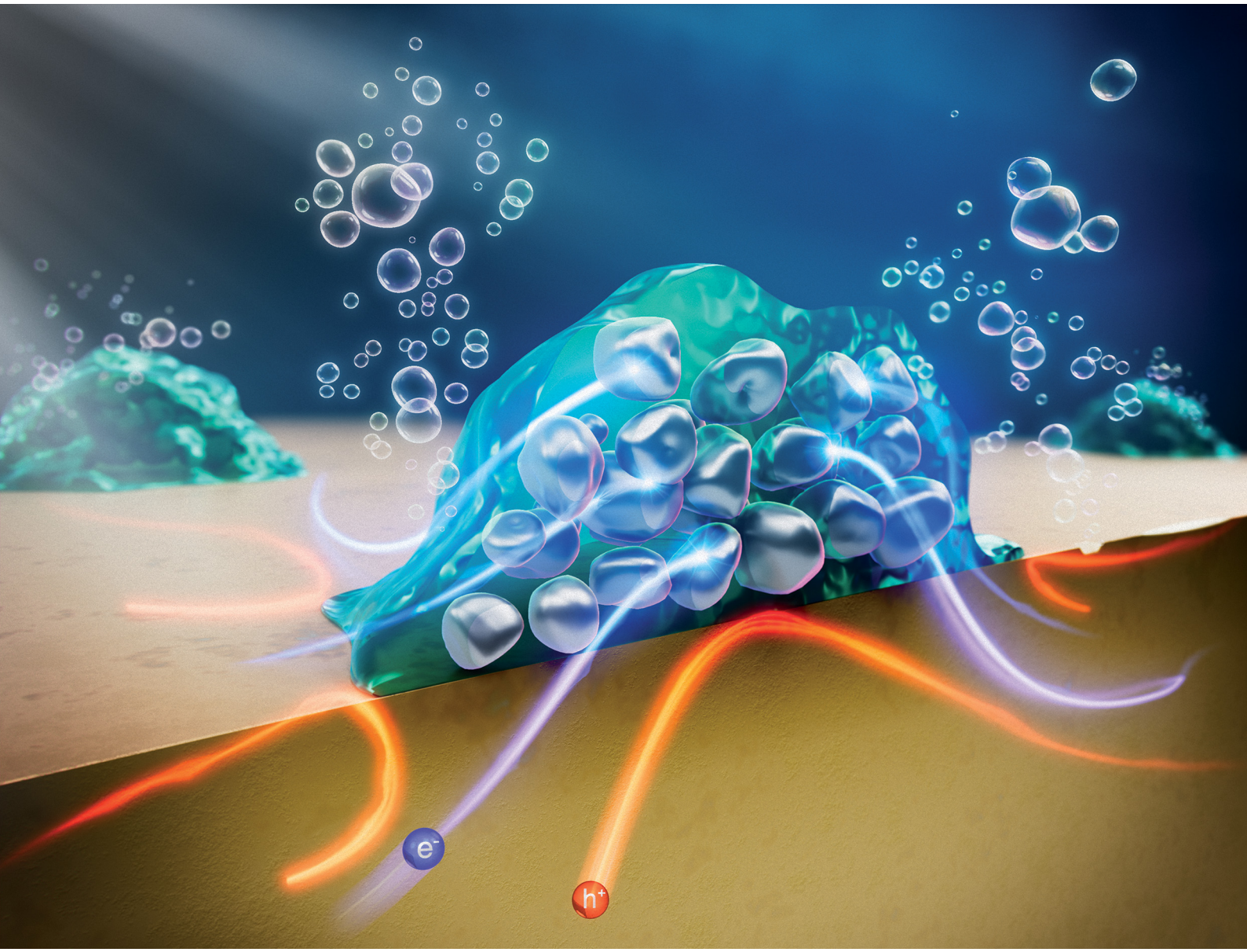

ISSN 2753-801X

ROYAL SOCIETY OF CHEMISTRY

PAPER

Ryu Abe *et al.*

An unexplored role of the CrO_x shell in an elaborated Rh/CrO_x core–shell cocatalyst for photocatalytic water splitting: a selective electron transport pathway from semiconductors to core metals, boosting charge separation and H_2 evolution

EES Catalysis

PAPER

View Article Online
View Journal | View Issue

Cite this: *EES Catal.*, 2023, 1, 255

An unexplored role of the CrO_x shell in an elaborated Rh/CrO_x core–shell cocatalyst for photocatalytic water splitting: a selective electron transport pathway from semiconductors to core metals, boosting charge separation and H_2 evolution†

Tetsu Kotani,‡[a] Kanta Ogawa,‡[a] Hajime Suzuki,[a] Kosaku Kato,[b] Osamu Tomita,[a] Akira Yamakata[b] and Ryu Abe*[a]

Received 20th December 2022,
Accepted 15th March 2023

DOI: 10.1039/d2ey00109h

rsc.li/eescatalysis

A core–shell structured Rh/CrO_x cocatalyst has endowed various semiconductors with high efficiency in water-splitting photocatalysis, where thin CrO_x layers on Rh have been assumed to be physical blockers of O_2 to the metal surface to suppress unfavorable reverse reactions (*e.g.*, catalytic H_2O formation from H_2 and O_2). Herein, we propose another unexplored but favorable function of CrO_x layers: a selective electron transport pathway from photocatalysts to the Rh core boosting charge separation and H_2 production. The subsequent loading of CrO_x layers onto Rh increased the rate of visible light H_2 evolution of a Bi_4NbO_8Cl photocatalyst, even in a half reaction with a hole scavenger where O_2 does not evolve. Transient absorption spectroscopy revealed that the CrO_x layer increases the electron path from Bi_4NbO_8Cl to Rh. Importantly, the highest H_2-evolution activity was obtained by simultaneous photodeposition using Cr^{III} and Rh^{III} precursors, which had not yet been examined. In this sample, Rh nanoparticles were enclosed by an amorphous CrO_x shell, where Rh particles were less directly attached to the semiconductor. Therein, CrO_x inserted between Bi_4NbO_8Cl and Rh effectively suppresses undesirable hole transfer from Bi_4NbO_8Cl to Rh, while such hole transfer partially occurs when they are in direct contact. These results indicated that CrO_x functions as a selective electron transport pathway and improves the H_2 evolution activity. Although the development strategy of cocatalysts has so far focused on surface redox reactions, this study offers a new approach for the design of highly efficient cocatalysts based on the carrier transfer process, especially at semiconductor–cocatalyst interfaces.

Broader context

Water splitting using a semiconductor photocatalyst enables clean hydrogen production from solar energy. Light irradiation excites electrons and holes in a photocatalyst. After their migration toward the surface of the photocatalyst, they participate in reduction and oxidation at reaction sites. Therefore, not only semiconductor photo-absorbers themselves, but also creating effective reaction sites on their surface is essential. Such a role can be played by "co-catalysts" on photocatalysts, the functions of which are generally (1) capturing either of photoexcited carriers from photocatalysts and (2) catalyzing redox reactions on the surface of photocatalysts. Although vast knowledge in electrocatalysis can be employed for the latter function, a versatile strategy has not yet been established for the former one. Here, we reveal that CrO_x in the Rh/CrO_x core–shell type cocatalyst helps in electron transfer from photocatalysts to the reaction sites (Rh). Rh/Cr_2O_3 is a widely used hydrogen evolution reaction cocatalyst in overall water splitting, where CrO_x has been considered to be a physical blocker of O_2 to the metal surface to suppress reverse reactions. We propose another function of CrO_x layers: a selective electron-transport pathway from photocatalysts to Rh, boosting charge separation and H_2 production. This study offers a new approach for designing cocatalysts based on the carrier transfer process.

[a] *Department of Energy and Hydrocarbon Chemistry, Graduate School of Engineering, Kyoto University, Nishikyo-ku, Kyoto, 615-8510, Japan. E-mail: ryu-abe@scl.kyoto-u.ac.jp*

[b] *Graduate School of Natural Science and Technology, Okayama University, 3-1-1 Tsushima-naka, Kita-ku, Okayama, 700-8530, Japan*

† Electronic supplementary information (ESI) available: SEM and TEM images, photocatalytic activity, and TA spectroscopy data. See DOI: https://doi.org/10.1039/d2ey00109h

‡ T. K. and K. O. contributed equally to this work.

Introduction

Highly efficient photocatalytic water splitting inevitably requires not only an efficient semiconductor photo-absorber but also effective cocatalysts.[1–5] In general, cocatalysts loaded on semiconductor photocatalysts play two crucial roles: (1) capturing

photoexcited carriers (either electrons or holes ideally) from the photocatalysts and (2) reducing the activation energy of target redox reactions on the surface of photocatalysts.[6] In terms of the latter role, vast knowledge accumulated in electrochemical catalysis for the hydrogen evolution reaction (HER) and the oxygen evolution reaction (OER) has provided us with useful principles for designing effective cocatalyst materials (*e.g.*, Pt for the HER and IrO_2 for the OER).[7] However, in terms of the former role, a versatile strategy has not yet been established for cocatalysts to capture photoexcited carriers selectively because metal–semiconductor interfacial charge transfer consists of highly complex processes.[8,9] Actually, even the most commonly used Pt cocatalyst captures photogenerated holes as well as photoexcited electrons in some cases, which causes undesirable charge recombination on Pt.[10–13] Therefore, photocatalytic water splitting systems with high efficiencies have been achieved based on the specially designed photocatalyst particles, where HER and OER cocatalysts are loaded on different crystal facets selectively by leveraging the photocatalytic deposition technique. Specifically, the Al-doped $SrTiO_3$ particle, which is synthesized using a flux method, possesses facet-dependent redox properties, and the photoexcited electrons accumulate on the {100} facet. Thus, it reduces metal cations to produce an HER cocatalyst (*i.e.*, Rh/Cr_2O_3) on that facet, while the photogenerated holes accumulate on the {110} facet, producing an OER cocatalyst oxidatively (*i.e.*, CoOOH) on it. Therefore, HER and OER cocatalysts selectively capture the photoexcited carriers that are desirable for photocatalytic water splitting. However, this strategy cannot be applied to other systems unless the photocatalyst material possesses a built-in and/or facet-dependent charge separation ability (*e.g.*, decahedral-shaped $BiVO_4$[14]).

The abovementioned Rh/Cr_2O_3 cocatalyst with a core–shell structure is one of the most widely used HER cocatalysts for achieving overall water splitting (*i.e.*, simultaneous evolution of H_2 and O_2) on various photocatalyst materials owing to its excellent resistance to reverse reactions.[4,15,16] Unfavorable reactions involving O_2 molecules, such as re-reduction of O_2 and/or catalytic formation of H_2O from H_2 and O_2 on conventional metallic HER cocatalysts (*e.g.*, Rh and Pt), are one of the major issues in photocatalytic water splitting. Domen *et al.* demonstrated that a thin layer of $Cr_2O_3{\cdot}nH_2O$ (denoted hereafter as CrO_x for brevity) coated on Rh (or Pt) effectively suppresses unfavorable reverse reactions on metal species because the layer is permeable to H^+ but not to O_2, preventing O_2 molecules from reaching the metal surface.[17]

Although the vital role of the CrO_x shell as a physical blocker of O_2 molecules has gained broad acceptance, we have noticed unaccountable results through our attempt to apply this Rh/CrO_x cocatalyst to a layered oxyhalide Bi_4NbO_8Cl photocatalyst possessing appropriate properties for visible-light water-splitting.[18] Specifically, the subsequent loading of CrO_x onto Rh increases the rate of H_2 evolution on Bi_4NbO_8Cl in the presence of methanol as a sacrificial electron donor, where O_2 does not evolve. In this study, we reveal an unexplored but favorable function of CrO_x layers as a selective electron transport pathway from photocatalysts to the Rh core (*i.e.*, reduction site), based on the results of varied Rh/CrO_x-type cocatalysts loaded on Bi_4NbO_8Cl, which were characterized by X-ray absorption near edge structure spectroscopy, X-ray photoelectron spectroscopy, transmission electron microscopy, and time-resolved spectroscopy.

Results and discussion

Photodeposition of Rh and CrO_x on Bi_4NbO_8Cl

Bi_4NbO_8Cl was synthesized using a flux method (Fig. S1, ESI†).[19] Rh and Cr species were loaded on Bi_4NbO_8Cl *via* photodeposition using Na_3RhCl_6, $Cr(NO_3)_3{\cdot}9H_2O$ (Cr^{III}), and K_2CrO_4 (Cr^{VI}) as precursors. Notably, the conventional core–shell Rh/CrO_x cocatalysts were prepared mostly *via* stepwise photoreduction by photoexcited electrons, where Rh^{III} species (*i.e.*, Na_3RhCl_6) were first reduced to form core Rh metal particles on the photocatalyst surface, and then Cr^{VI} species (K_2CrO_4) were reduced to Cr^{III} species by the electrons that accumulate on the Rh to form a shell on the Rh surface. It has been suggested that the shell layers formed on Rh mainly consist of a mixture of $Cr_2O_3{\cdot}nH_2O$, while we herein describe them as CrO_x for simplicity, as in previous reports.[20] In addition to the high-valent Cr^{VI} precursor, we employed another precursor, $Cr(NO_3)_3$, containing low-valent (Cr^{III}) species. This is based on the expectation that the hydroxide ions (OH^-) produced *via* the photocatalytic reduction of NO_3^- on Rh ($NO_3^- + H_2O + 2e^- \rightarrow NO_2^- + 2OH^-$) can react with the Cr^{III} species to produce $Cr(OH)_3$, finally forming CrO_x-like species on the surface of the Rh core, as demonstrated in the coating of photocatalyst surface with CrO_x-like layers.[21] The samples prepared *via* the stepwise method using Cr^{III} and Cr^{VI} will be hereafter denoted as Rh/Cr^{III} and Rh/Cr^{VI}, respectively. Herein, we also employed simultaneous deposition in which the photocatalyst particles were irradiated in a solution containing both Rh and Cr precursors (denoted as $Rh + Cr^{III}$ or $Rh + Cr^{VI}$). To the best of our knowledge, simultaneous deposition using Cr^{III} as a precursor has not been investigated so far, while that with Cr^{VI} has been reported.[22]

Fig. 1 shows the Rh–K and Cr–K edge XANES spectra of the prepared samples. All the samples, except for $Rh + Cr^{VI}$, were confirmed to consist of the Rh metal species based on a comparison with the spectrum of the Rh metal foil. The spectrum of the $Rh + Cr^{VI}$ sample resembles that of the reference Rh_2O_3, indicating the insufficient reduction of the Rh precursor by photoexcited electrons. This is probably due to the preferential reduction of Cr^{VI} ($CrO_4^{2-} + 5H^+ + 3e^- \rightleftarrows Cr(OH)_3 + H_2O$; $E^\circ = 1.386$ V). The Cr–K spectra of all prepared samples were in good agreement with that of the reference $Cr_2O_3{\cdot}nH_2O$ (Fig. 1b) sample, as well as with previous data on CrO_x loaded GaN:ZnO.[17,23] The EXAFS spectra further supported this conclusion (Fig. S2, ESI†). A trivalent Cr species is also observed by the X-ray photoelectron spectroscopy (XPS) analysis (Fig. S3, ESI†).

As shown in Fig. 2a, Rh particles were deposited as agglomerates with a size of approximately 20 nm when Rh was solely loaded on Bi_4NbO_8Cl; the lattice fringes ensured the zero-valent

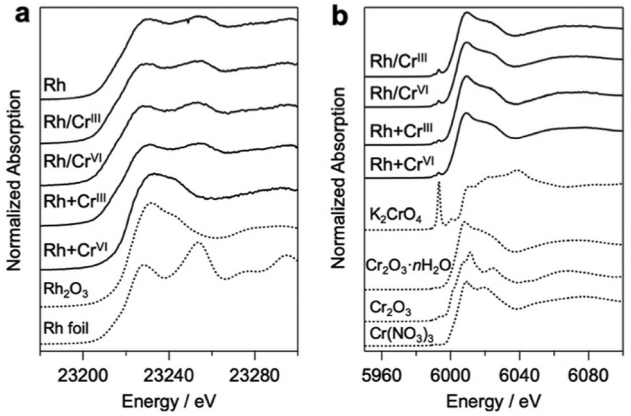

Fig. 1 (a) Rh–K and (b) Cr–K edge XANES spectra of Rh and Cr-loaded Bi_4NbO_8Cl prepared *via* stepwise (Rh/Cr^{III}, Rh/Cr^{VI}) and simultaneous deposition ($Rh + Cr^{III}$, $Rh + Cr^{VI}$). The reference samples are shown as dotted lines. $Cr_2O_3{\cdot}nH_2O$ was obtained *via* a precipitation reaction where NaOH was added to a $Cr(NO_3)_3$ solution.

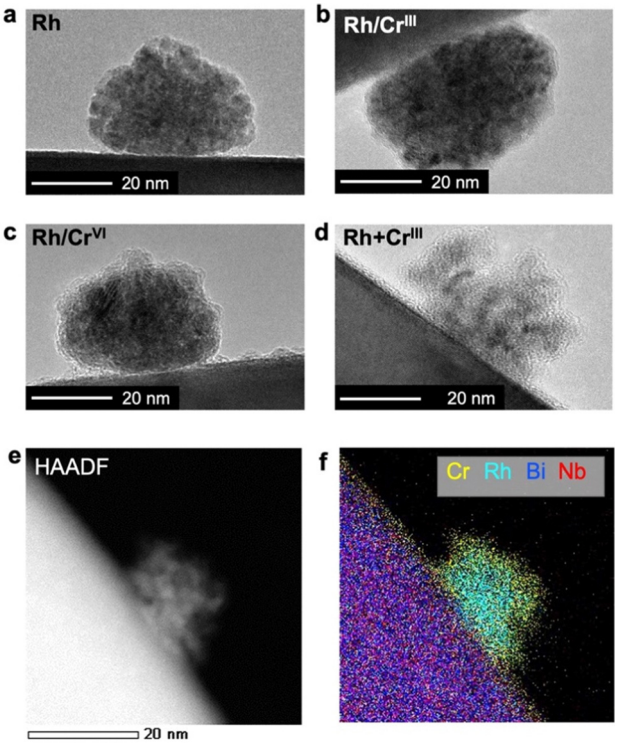

Fig. 2 HR-TEM images of cocatalysts loaded on (a) Rh, (b) Rh/Cr^{III}, (c) Rh/Cr^{VI}, and (d) $Rh + Cr^{III}$ samples. (e) HAADF-STEM and (f) EDX elemental mapping images of the $Rh + Cr^{III}$ sample.

state of Rh (Fig. S4, ESI†). Stepwise loading of the Cr precursor (Rh/Cr^{III} and Rh/Cr^{VI}) formed an amorphous CrO_x layer (Fig. 2b and c) while maintaining the morphology and size of the Rh core. HAADF-STEM and EDX elemental mapping images confirmed the Rh/Cr core/shell structure (Fig. S5 and S6, ESI†). In stark contrast, the simultaneous deposition of the Cr^{III} precursor ($Rh + Cr^{III}$) provided differently shaped particles, where Rh of a few nanometer size was enclosed by an amorphous CrO_x shell (Fig. 2d–f and Fig. S7, ESI†). In each case, an easier reduction reaction on Rh than on the bare surface of Bi_4NbO_8Cl may contribute to CrO_x growth around Rh nanoparticles. Although some large particles were also observed (Fig. S8, ESI†), their number was small (less than 5.2% of the observed 200 particles). As for $Rh + Cr^{VI}$, only amorphous particles were deposited (Fig. S4, ESI†), which may be Rh^{III}–Cr^{III} mixed-oxides by considering the XANES spectra (Fig. 1a).[22,24]

Impact of the CrO_x shell on the H_2 evolution activity of the Rh-loaded Bi_4NbO_8Cl photocatalyst

H_2 evolution activities of the prepared samples were evaluated in an aqueous methanol solution (MeOH aq.) where the photoexcited electrons and holes are expected to react with water (or H^+) and methanol, respectively. Fig. 3 shows the time courses of H_2 evolution on various samples under visible light irradiation ($\lambda > 400$ nm). The first noteworthy fact is that the coating of Rh with the CrO_x shell enhanced H_2 evolution; the Rh/Cr^{III} and Rh/Cr^{VI} samples showed higher rates than Rh. The sample with CrO_x randomly deposited *via* the impregnation method instead of the photodeposition method showed a lower H_2 evolution activity, which supports the function of the CrO_x layer on Rh (Fig. S9, ESI†). The second and most important finding of this study is that the $Rh + Cr^{III}$ sample prepared *via* the unexplored simultaneous photodeposition of Rh^{III} and Cr^{III} precursors showed a significantly higher activity than the Rh-solely loaded and other CrO_x-coated samples. The negligible activity of $Rh + Cr^{VI}$ prepared *via* simultaneous photodeposition of Rh^{III} and Cr^{VI} can be due to the insufficient reduction of the Rh^{III} precursor, as indicated by the Rh K-edge XANES spectra (see Fig. 1).

The enhancement in the H_2-evolution reaction by CrO_x coating on Rh cannot be explained by the widely accepted role of the CrO_x shell as a physical blocker of O_2 molecules because O_2 evolution should not take place in the presence of an efficient hole scavenger, methanol. One possible factor is the deactivation of the Rh metal surface by some intermediates generated from methanol, such as formaldehyde, as suggested in the case of the Pt cocatalyst loaded on TiO_2.[25] However, H_2 evolution on the Rh-loaded sample remained unchanged even in the presence of formaldehyde (Fig. S10, ESI†) in MeOH (aq.), which eliminates this possibility. The Bi_4NbO_8Cl sample loaded solely with CrO_x species (*via* photodeposition of the Cr^{VI} precursor) did not show detectable H_2 evolution from MeOH (aq.) under visible light irradiation (Fig. S11, ESI†), indicating negligible activity of CrO_x as an HER cocatalyst.[20,26] In addition, no H_2 was generated over Rh-loaded $Cr_2O_3{\cdot}nH_2O$ (*i.e.*, in the absence of the Bi_4NbO_8Cl photocatalyst, see Fig. S12, ESI†), confirming the negligible activity of CrO_x itself as a semiconductor photocatalyst under the present reaction conditions. The promotion of H_2 evolution from MeOH (aq.) by CrO_x-coating on Rh (prepared *via* simultaneous photodeposition of Rh^{III} and Cr^{III} precursors) was also observed on a conventional water-splitting photocatalyst $SrTiO_3$ under UV light irradiation (Fig. 6), which demonstrates that this unexplored effect of the CrO_x shell is not specific to the Bi_4NbO_8Cl photocatalyst.

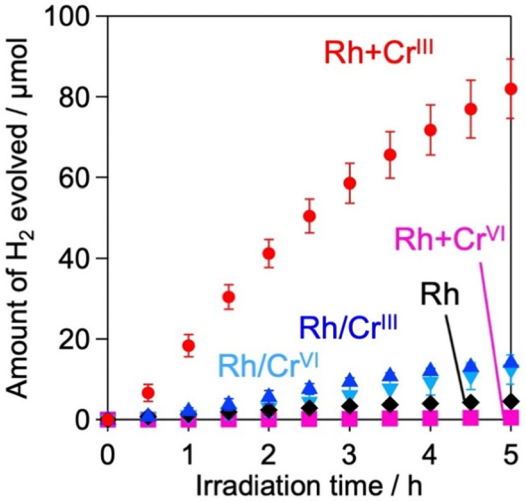

Fig. 3 Time courses of H_2 evolution of Rh (black), Rh/Cr^{III} (blue), Rh/Cr^{VI} (light blue), Rh + Cr^{III}, (red), and Rh + Cr^{VI} (pink) samples. The reactions were conducted in an aqueous methanol solution (20 vol%, 250 mL) under visible light irradiation ($\lambda > 400$ nm). Error bars signify the standard deviation.

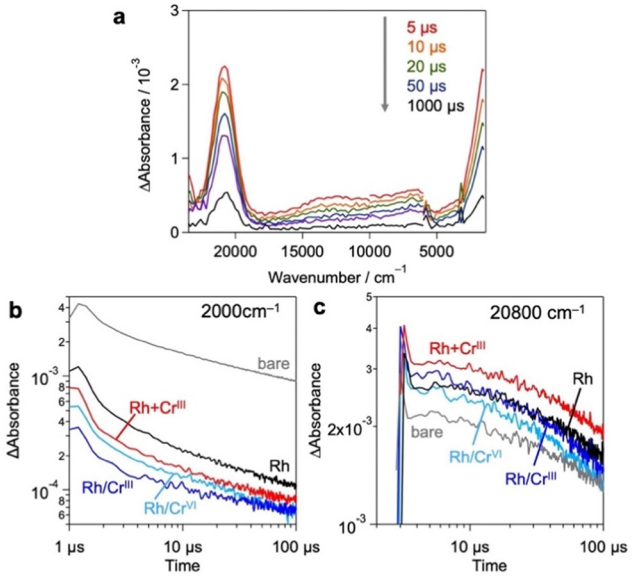

Fig. 4 (a) TA spectra of bare Bi_4NbO_8Cl after excitation. (b and c) Decay kinetics of the transient absorption in the μ-second regions measured at (b) 2000 cm^{-1} and (c) 20 800 cm^{-1} in N_2 (20 torr). The samples were excited by UV laser pulses (355 nm).

Previous studies have reported enhanced H_2 evolution from MeOH (aq.) by CrO_x shells on Rh for GaN:ZnO and $SrTiO_3$, while the detailed mechanism for enhancement has not been discussed.[17,27] These facts strongly suggest the presence of a previously unknown function of the CrO_x shell in enhancing H_2 evolution (*i.e.*, reduction of H^+ and/or water), in addition to its function as a physical blocker.

Spectroscopic elucidation of the unexplored function of the CrO_x shell

Based on these results and previous reports that CrO_x does not to promote the catalytic HER,[20,26] we focused on the effect of the loaded CrO_x on the charge carrier (either electrons or holes) transfer process rather than the catalytic process in photocatalysis.[20,26] We employed transient absorption (TA) spectroscopy[28–30] to evaluate the effect of CrO_x on the carrier dynamics between a photocatalyst (Bi_4NbO_8Cl) and its catalytic site (Rh). Fig. 4a shows the TA spectra of bare Bi_4NbO_8Cl, where bandgap excitation induces two absorption increases in the infrared (IR) (2000 cm^{-1}) and visible (20 800 cm^{-1}) regions. Referring to previous results (*e.g.*, TiO_2,[31–33] α-Fe_2O_3[34] and $LaTiO_2N$[28]), the IR features have been attributed to photogenerated free electrons in the conduction band (CB) and/or shallowly trapped electrons,[35,36] while the visible features have been associated with photogenerated holes.[29,30]

Fig. 4b and c show the decay kinetics of the IR (2000 cm^{-1} for electrons) and visible (20 800 cm^{-1} for holes) regions, respectively, for the various samples. Compared to the bare Bi_4NbO_8Cl, the sole loading of Rh metal species decreased the signal intensity of electrons but increased that of holes, indicating the preferential capture of photoexcited electrons by Rh, as reported previously.[13] The deposition of CrO_x shells on the Rh-loaded Bi_4NbO_8Cl (Rh/Cr^{III} and Rh/Cr^{VI}) further decreased the electron signal but had little impact on the hole signal. Given the fact that the CrO_x shells on the pre-loaded Rh increased the rate of H_2 evolution despite the inertness of CrO_x for the HER,[20,26] it appears that CrO_x captures the photoexcited electrons from Bi_4NbO_8Cl, transfers them to the Rh core, and consequently increases the number of electrons for the HER. More importantly, in the Rh + Cr^{III} sample, which shows the highest H_2 evolution activity, the signal of holes was further increased compared to that of the Rh-loaded sample, whereas the electron signal was decreased as with the case of Rh/Cr^{III} and Rh/Cr^{VI}. This phenomenon suggests that the charge separation between the holes on Bi_4NbO_8Cl and the electrons on Rh was further improved by the CrO_x species loaded *via* the unexplored simultaneous photodeposition of the Rh^{III} and Cr^{III} precursors, which is consistent with the highest H_2 evolution activity of this sample. In other words, the function of CrO_x, selective electron transfer from Bi_4NbO_8Cl to Rh, was more apparent in this sample. A similar tendency was also observed in an earlier process on a pico-second scale (Fig. S13, ESI†).

The electron-selective capturing ability of the CrO_x shell was further supported by the TA values of the bare and CrO_x-loaded Bi_4NbO_8Cl samples. As shown in Fig. S15 (ESI†), CrO_x loading on the bare Bi_4NbO_8Cl surface significantly decreased the IR signal but increased the visible signal. These results on TA measurements strongly suggest that the CrO_x species can selectively capture photoexcited electrons from Bi_4NbO_8Cl, prolonging the lifetime of the holes by promoting the spatial separation of electrons and holes.

Mechanism for significant enhancement in H_2 production on the Rh/CrO_x cocatalyst

Based on the above results (physicochemical properties, photocatalytic activity, and carrier dynamics), we now propose a previously unknown function of the CrO_x shell as an electron

transport layer between the semiconductor and the Rh core, as illustrated in Fig. 5.

In the Rh/Cr^{III} and Rh/Cr^{VI} samples, where CrO_x was subsequently photodeposited on the pre-loaded Rh, the CrO_x layers, as well as the Rh directly attached to Bi_4NbO_8Cl, capture the photoexcited electrons from Bi_4NbO_8Cl, serving as an electron path between Bi_4NbO_8Cl and Rh (Fig. 5a). Therefore, the CrO_x layer on Rh facilitated electron transfer to Rh, increasing the number of electrons participating in H^+ reduction on Rh, enhancing H_2 evolution. Notably, a much higher H_2 evolution rate was observed for the Rh + Cr^{III} sample, where most of the Rh nanoparticles were enclosed by an amorphous CrO_x shell, and the contact area between Rh and Bi_4NbO_8Cl was much smaller than that of the other samples (Fig. 2 and Fig. S8, ESI†). Given the TA results indicating the electron-selective capturing ability of CrO_x, the CrO_x intermediate between Bi_4NbO_8Cl and Rh in Rh + Cr^{III} selectively passed electrons, thus boosting H_2 evolution (Fig. 5b). Although undesirable hole transfer from Bi_4NbO_8Cl to Rh partially occurs when they are in direct contact with each other, as in the case of Pt,[10–13] the insertion of the electron-selective pathway of CrO_x effectively suppresses this hole transfer and therefore the problematic charge recombination at the semiconductor–metal interfaces. The function of CrO_x as an electron-selective pathway was further supported by the enhanced H_2 evolution on the sample where CrO_x was first deposited on Bi_4NbO_8Cl followed by the Rh species (Fig. S16, ESI†). The sample showed a much higher activity than the Rh-loaded one despite the incomplete reduction to metal and agglomerated morphology of the Rh species, indicating the effectiveness of CrO_x for improving the carrier transfer process.

The function of the CrO_x shell as a "selective" electron transport layer is similar to those employed in solar cells to suppress charge recombination.[37] Indeed, some chromium oxide species have been reported to serve as an electron transport layer between a semiconductor photo-absorber (*e.g.*, lead-halide perovskite solar cells) and an electrode (*e.g.*, fluorine-doped tin oxide (FTO) and Ag substrates).[38,39] Generally, the function of an electron transport layer can be explained based on the band alignment among three components (*i.e.*, photo-absorber, electron transport layer, and conductive electrode). The band levels of the CrO_x species were estimated using a combination of diffuse reflectance spectroscopy and photoelectron yield spectroscopy (Fig. S17, ESI†). $Cr_2O_3{\cdot}nH_2O$ particles were prepared *via* a precipitation method in which OH^- was added to the solution containing Cr^{3+} ions to imitate the photodeposition process of CrO_x from Cr^{3+} on Bi_4NbO_8Cl. The Cr–K edge XANES of the sample confirmed the formation of almost the same species as that loaded on Bi_4NbO_8Cl. Fig. 5c shows the estimated band alignments for Bi_4NbO_8Cl, $Cr_2O_3{\cdot}nH_2O$, and Rh. The CBM (Cr-3d*)[40] position of $Cr_2O_3{\cdot}nH_2O$ was favorable for receiving electrons generated in the CBM of Bi_4NbO_8Cl and injecting them into Rh. Given the band alignment, the holes, not only electrons, can transfer to $Cr_2O_3{\cdot}nH_2O$. However, the driving force (energy difference between the VBM and Cr-3d) is much smaller than that for the electrons (from the CBM to Cr-3d*), which is probably one of the origins of the preferred electron transfer in addition to other factors such as donor or acceptor density of the present CrO_x species. In other words, the driving force of hole transfer (work function difference) from Bi_4NbO_8Cl to Rh (about 1.55 eV) can be reduced to 0.07 eV by introducing the CrO_x layer, which can suppress the undesirable hole transfer from the photocatalyst to Rh.

From these results, we conclude that CrO_x functions as a selective electron transport layer, promoting charge separation between the photocatalyst and noble metal reaction sites, thus boosting H_2 evolution. The significant improvement in H_2 evolution indicates that the CrO_x layers formed *via* the present procedure (*i.e.*, simultaneous photodeposition) possess substantial permeability to H^+ (or other related species such as H_3O^+), as proposed in previous reports on conventional Rh/CrO_x cocatalysts.[4,15,16] Another important question arises: whether the CrO_x layers formed *via* the present procedure can function as a physical blocker against O_2 molecules, which will be discussed later.

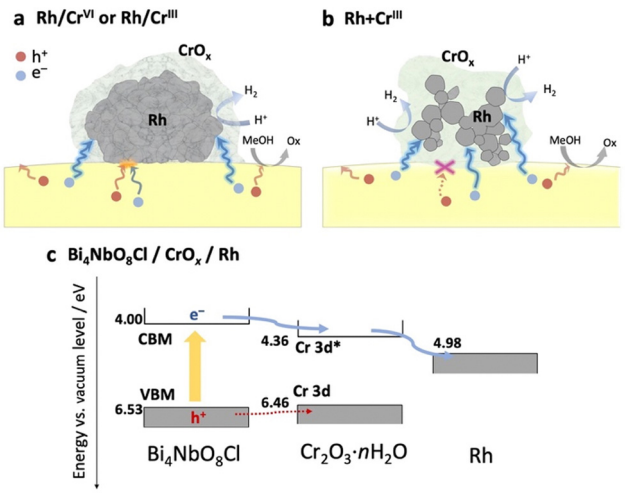

Fig. 5 Schematic of the role of CrO_x in the carrier transfer process from the semiconductor photocatalyst to Rh in (a) Rh/Cr^{III} (or Rh/Cr^{VI}) and (b) Rh + Cr^{III}. (c) Energy level diagram for Bi_4NbO_8Cl, $Cr_2O_3{\cdot}nH_2O$, and Rh.

Applicability of the CrO_x layers formed *via* simultaneous deposition to other systems

The significant impact of CrO_x layers on H_2 evolution was also confirmed for other metal cores and semiconductors, as it was not specific to the combination of the Rh core and Bi_4NbO_8Cl. As for metal cores, we have previously revealed that conventional Pt cocatalysts cannot boost H_2 production on Bi_4NbO_8Cl because Pt captures both electrons and holes, acting as a recombination center[13] as shown in Fig. S18 (ESI†). When Pt and Cr species were simultaneously loaded on Bi_4NbO_8Cl (Pt + Cr^{III}), most of the Pt particles were encapsulated by amorphous CrO_x (Fig. S19 and S20, ESI†), as in the case of Rh + Cr^{III}. The Pt + Cr^{III} sample showed much improved H_2 evolution compared to the Pt sample, which strongly suggests that the CrO_x layer also helps selective electron transfer from Bi_4NbO_8Cl to Pt (Fig. S21, ESI†).

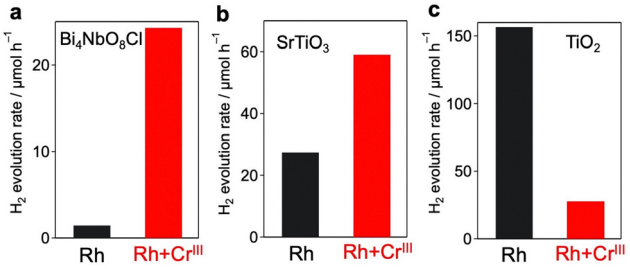

Fig. 6 Effect of co-deposition of CrO_x with Rh on the photocatalytic activity of (a) Bi_4NbO_8Cl ($\lambda > 400$ nm), (b) $SrTiO_3$ ($\lambda > 300$ nm), and (c) rutile TiO_2 ($\lambda > 300$ nm).

The simultaneous photodeposition of CrO_x and Rh on $SrTiO_3$ (Rh + Cr^{III}) also provides a higher H_2 evolution rate from MeOH (aq.) compared to Rh-loaded $SrTiO_3$ (Fig. S22, ESI†), whereas the enhancement was moderate compared to that of Bi_4NbO_8Cl (Fig. 6 and Table S3, ESI†). In contrast, the co-deposition of CrO_x significantly lowered the H_2 evolution rate of Rh-loaded rutile TiO_2 (Fig. S24, ESI†) from MeOH (aq.). This stark contrast may support the abovementioned electron-transfer mechanism. Since the CBM level of $SrTiO_3$ (*ca.* 4.2 eV against the vacuum level) is almost the same as that of Bi_4NbO_8Cl and higher than that of CrO_x, the electron transfer from $SrTiO_3$ to Rh through CrO_x layers can be rationalized (see Fig. S25, ESI†). On the other hand, the CBM of rutile TiO_2 is lower (*ca.* 4.37 eV against the vacuum level) than that of Bi_4NbO_8Cl and quite similar to that of CrO_x, making the driving force of the electron transfer through the conduction band of CrO_x almost negligible.

As noted in the Introduction, the main role of the CrO_x layer has been regarded as a physical blocker of O_2 molecules to suppress reverse reactions such as water formation (from H_2 and O_2) and O_2 reduction on noble metal cocatalysts. To investigate the role of the CrO_x layers prepared *via* simultaneous photodeposition (*i.e.*, Rh + Cr^{III}), overall water splitting was performed using the $SrTiO_3$ photocatalyst. As shown in Fig. S26 (ESI†), while the Rh-loaded $SrTiO_3$ without CrO_x does not show stoichiometric water splitting due to the undesirable reaction with O_2 molecules on the exposed Rh,[6] simultaneous CrO_x deposition provided stoichiometric water splitting, which confirms the role of the CrO_x shell as a physical blocker. Notably, the sample prepared using the present method (Rh + Cr^{III}) showed slightly higher photocatalytic activity than the sample prepared using the conventional method (Rh/Cr^{VI}). Unfortunately, we have not yet succeeded in splitting pure water into H_2 and O_2 using the Bi_4NbO_8Cl samples loaded with these Rh/CrO_x cocatalysts, probably because of the insufficient optimization of other factors such as the loading of an effective O_2-evolution cocatalyst, which will be our future work.

Conclusions

In summary, we demonstrated that CrO_x facilitates the transfer of photoexcited electrons from a photocatalyst to a noble metal reduction site. The CrO_x layer on the pre-loaded Rh served as an electron path, facilitating electron transfer from the Bi_4NbO_8Cl photocatalyst to Rh, which resulted in improved H_2 evolution activity under visible light. Notably, when Rh and CrO_x are loaded simultaneously *via* photodeposition using a Cr^{3+} precursor, CrO_x lies between Rh and Bi_4NbO_8Cl. Therein, the CrO_x layer passes only electrons to Rh, suppressing undesirable hole transfer to Rh, which further improves the activity. Thus far, the facilitation of surface reactions (*e.g.*, the HER and OER) has mainly been investigated as a function of the cocatalysts. However, we revealed the crucial role of CrO_x in the carrier transfer process from the photocatalyst to the catalyst (reaction site). We believe that the precise control of the physicochemical properties of Cr species by doping,[41] making solid solutions with other transition metal compounds,[40] and employing other ligands (anions)[42,43] will reveal more detailed dynamics in the carrier transport process from photocatalysts to noble metals to suppress the undesirable charge recombination more effectively. Employing other semiconductors having appropriate band edge positions as electron transport layers will also be an effective choice. This study offers a new approach for designing cocatalysts based on their carrier-capturing abilities.

Experimental

Materials

Bi_2O_3 (99.99%), BiOCl (95.0%), Nb_2O_5 (99.9%), NaCl (99.5%), CsCl, methanol (99.8%), Rh_2O_3 (98.0%), K_2CrO_4 (99.0%), CrO_3(99.5%), $H_2PtCl_6{\cdot}6H_2O$ (99.9%), PtO_2 (98.0%), and BN were purchased from FUJIFILM Wako Pure Chemicals. $Na_3RhCl_6{\cdot}nH_2O$ (80.0%), $Cr(NO_3)_3{\cdot}9H_2O$ (98.0%), and Cr_2O_3 (98.5%) were purchased from Kanto Chemical. $SrTiO_3$ (99%) was purchased from Sigma-Aldrich. TiO_2 (rutile, 99.99%) was purchased from High Purity Chemicals. Formaldehyde solution (37%) was purchased from Nacalai Tesque. The compound described as $Cr_2O_3{\cdot}nH_2O$ was obtained from the precipitate formed by the addition of NaOH to the $Cr(NO_3)_3$ solution.

Synthesis of Bi_4NbO_8Cl using the flux method

Bi_4NbO_8Cl was synthesized using the flux method, as reported in our previous work.[19] Briefly, a stoichiometric mixture of Bi_2O_3, BiOCl, and Nb_2O_5 was mixed with flux (NaCl and CsCl in the molar ratio of 35 : 65) at 1 mol%. The mixture (25 g) was placed in a 30 mL alumina crucible, heated at a rate of 50 °C h^{-1} to 650 °C, and held at the final temperature for 10 h. The product was naturally cooled to room temperature, thoroughly washed with distilled water, filtered, and air-dried. The obtained powder was confirmed to be Bi_4NbO_8Cl by X-ray diffraction (XRD).

Loading of the co-catalyst

The prepared Bi_4NbO_8Cl (0.2 g) was dispersed in an aqueous methanol solution (20 vol%, 250 mL). Depending on the preparation conditions, the Rh precursor ($Na_3RhCl_6{\cdot}nH_2O$), Pt precursor ($H_2PtCl_6{\cdot}6H_2O$), and/or Cr precursor ($Cr(NO_3)_3{\cdot}9H_2O$

or K_2CrO_4) were added to the solution. The amount of precursor added was 1.0 wt% for Rh (or Pt) and 1.5 wt% for Cr as a metal cation (Fig. S20, ESI†). After degassing, the solution was irradiated with visible light ($\lambda > 400$ nm) for 5 h at room temperature under continuous stirring. Irradiation was conducted using a 300 W Xe lamp equipped with a CM1 cold mirror and an L-42 cutoff filter. The product was filtered, washed thoroughly with distilled water, and air-dried. Absorption spectroscopy ensured that precursors for the Rh were fully consumed during the PD process, while the loading amounts of Cr were approximately 0.6, 1.3, and 1.3 wt% for Rh/Cr^{VI}, Rh/Cr^{III}, and Rh + Cr^{III}, respectively (Fig. S28, ESI†).

CrO_x was also loaded using the impregnation method. A certain amount of Rh/Bi_4NbO_8Cl powder was immersed in an aqueous solution containing $Cr(NO_3)_3$ (1.5 wt%). The suspension was evaporated under constant stirring until achieving complete dryness, followed by heating under an Ar flow at 150 °C.

Characterization

The prepared samples were studied by X-ray absorption fine structure (XAFS) spectroscopy, X-ray photoelectron spectroscopy (XPS), transmission electron microscopy (TEM), and scanning electron microscopy (SEM). XAFS measurements were carried out at the AR-NW10A, BL9C, and BL12C beamlines of the Photon Factory (High Energy Accelerator Research Organization, Tsukuba, Japan). The X-ray energy was varied using a Si(111) double-crystal monochromator. The reference samples were diluted in boron nitride, compressed to form pellets (except for Rh foil), and measured in the transmission mode. Cocatalyst-loaded samples were measured in fluorescence mode using a multichannel solid-state detector. XPS measurements were carried out with 5500MT (ULVAC-PHI) using Mg Kα as the X-ray source. The spectra were calibrated with the $4f_{7/2}$ peak (84.0 eV) of Au deposited on the sample surface using a magnetron sputtering device (MSP-1S). TEM and SEM were conducted using a JEM-2100F (JEOL) and an Nvision 40 (Zeiss), respectively.

Photocatalytic reaction

The photocatalytic reactions were performed in a closed circulation system. The sample (0.1 g) was dispersed in an aqueous methanol solution (20 vol%, 250 mL) in a Pyrex reaction vessel. After degassing, the solution was irradiated using a 300 W Xe lamp at room temperature with continuous stirring. In the case of Bi_4NbO_8Cl, the sample was irradiated (visible light ($\lambda > 400$ nm)) using a CM1 cold mirror and an L-42 cutoff filter. The evolved gases were analyzed using a gas chromatograph (GC-8A, SHIMADZU) with a thermal conductivity detector (TCD) using Ar as the carrier gas.

Transient absorption (TA) measurements

TA measurements were performed using a custom-built spectrometer as previously described. Briefly, for microsecond measurements, samples fixed on a CaF_2 plate were excited by a 355 nm laser pulse (0.5 mJ pulse energy, 0.5–1 Hz repetition rate). As a probe light, visible to near-IR light (25 000–6000 cm^{-1}) was irradiated from a halogen lamp and mid-IR light (6000–1000 cm^{-1}) was irradiated from the $MoSi_2$ coil. The transmitted or diffuse reflected probe light monochromated using a spectrometer was detected using Si, InGaAs, and MCT detectors in the visible, near-IR, and mid-IR regions, respectively. Picosecond measurements were performed using a Ti:sapphire laser system (Spectra-Physics, Solstice & TOPAS Prime; 90 fs duration; 500 Hz repetition rate). To excite the samples, 355 nm pulses (6 μJ pulse energy) were used. The probes 20 800 cm^{-1} and 2000 cm^{-1} were detected using a photomultiplier and an MCT detector, respectively. All the TA measurements were performed under N_2 (20 torr). The bare Bi_4NbO_8Cl sample used here was irradiated in a methanol solution in advance to obtain a light irradiation history similar to that of other photodeposited samples.

Author contributions

Tetsu Kotani: data curation, investigation, methodology visualization, and writing – original draft. Kanta Ogawa: conceptualization, investigation, methodology, and writing – original draft. Hajime Suzuki: writing – review & editing. Kosaku Kato: investigation. Osamu Tomita: investigation. Akira Yamakata: resources and data curation. Ryu Abe: resources, supervision, and writing – review & editing.

Conflicts of interest

There are no conflicts to declare.

Acknowledgements

This work was financially supported by the JST-CREST project, the JSPS KAKENHI Grant-in-Aid for Scientific Research (A) (JP20H00398), the JSPS KAKENHI Grant Number 17H06439 for Scientific Research on Innovative Areas "Innovations for Light-Energy Conversion (I4LEC)," the JSPS Research Fellowship (Grant Number 19J23357), and the JSPS Core-to-Core Program (JPJSCCA20200004). This work was also supported by the Iketani Science and Technology Foundation and the TEPCO Memorial Foundation. A part of this work was supported by the Advanced Research Infrastructure for Materials and Nanotechnology in Japan (JPMXP1222KU0026). We acknowledge Prof. Shunsuke Nozawa of KEK for his helpful support in XAFS measurement. We are also grateful to Takaaki Toriyama of Kyushu University for his helpful support in the STEM analysis.

Notes and references

1 R. Abe, *Bull. Chem. Soc. Jpn.*, 2011, **84**, 1000–1030.
2 M. R. Shaner, H. A. Atwater, N. S. Lewis and E. W. McFarland, *Energy Environ. Sci.*, 2016, **9**, 2354–2371.
3 R. Bala Chandran, S. Breen, Y. Shao, S. Ardo and A. Z. Weber, *Energy Environ. Sci.*, 2018, **11**, 115–135.

4 T. Takata, J. Jiang, Y. Sakata, M. Nakabayashi, N. Shibata, V. Nandal, K. Seki, T. Hisatomi and K. Domen, *Nature*, 2020, **581**, 411–414.
5 Y. Shang, T. Wang, Y. Xiao, Z. Dong, X. Li and B. Li, *J. Alloys Compd.*, 2021, **875**, 159998.
6 K. Maeda and K. Domen, *Bull. Chem. Soc. Jpn.*, 2016, **89**, 627–648.
7 A. Kudo and Y. Miseki, *Chem. Soc. Rev.*, 2009, **38**, 253–278.
8 V. Subramanian, E. E. Wolf and P. V. Kamat, *J. Am. Chem. Soc.*, 2004, **126**, 4943–4950.
9 K. Wu, H. Zhu, Z. Liu, W. Rodríguez-Córdoba and T. Lian, *J. Am. Chem. Soc.*, 2012, **134**, 10337–10340.
10 M. Yoshida, A. Yamakata, K. Takanabe, J. Kubota, M. Osawa and K. Domen, *J. Am. Chem. Soc.*, 2009, **131**, 13218–13219.
11 S. Schäfer, S. A. Wyrzgol, R. Caterino, A. Jentys, S. J. Schoell, M. Hävecker, A. Knop-Gericke, J. A. Lercher, I. D. Sharp and M. Stutzmann, *J. Am. Chem. Soc.*, 2012, **134**, 12528–12535.
12 F. Yan, Y. Wang, J. Zhang, Z. Lin, J. Zheng and F. Huang, *ChemSusChem*, 2014, **7**, 101–104.
13 K. Ogawa, R. Sakamoto, C. Zhong, H. Suzuki, K. Kato, O. Tomita, K. Nakashima, A. Yamakata, T. Tachikawa, A. Saeki, H. Kageyama and R. Abe, *Chem. Sci.*, 2022, **13**, 3118–3128.
14 R. Li, F. Zhang, D. Wang, J. Yang, M. Li, J. Zhu, X. Zhou, H. Han and C. Li, *Nat. Commun.*, 2013, **4**, 1432.
15 Z. Wang, Y. Inoue, T. Hisatomi, R. Ishikawa, Q. Wang, T. Takata, S. Chen, N. Shibata, Y. Ikuhara and K. Domen, *Nat. Catal.*, 2018, **1**, 756–763.
16 Q. Wang, M. Nakabayashi, T. Hisatomi, S. Sun, S. Akiyama, Z. Wang, Z. Pan, X. Xiao, T. Watanabe, T. Yamada, N. Shibata, T. Takata and K. Domen, *Nat. Mater.*, 2019, **18**, 827–832.
17 K. Maeda, K. Teramura, D. Lu, N. Saito, Y. Inoue and K. Domen, *J. Phys. Chem. C*, 2007, **111**, 7554–7560.
18 H. Fujito, H. Kunioku, D. Kato, H. Suzuki, M. Higashi, H. Kageyama and R. Abe, *J. Am. Chem. Soc.*, 2016, **138**, 2082–2085.
19 K. Ogawa, A. Nakada, H. Suzuki, O. Tomita, M. Higashi, A. Saeki, H. Kageyama and R. Abe, *ACS Appl. Mater. Interfaces*, 2019, **11**, 5642–5650.
20 M. Qureshi, T. Shinagawa, N. Tsiapis and K. Takanabe, *ACS Sustainable Chem. Eng.*, 2017, **5**, 8079–8088.
21 S. Chu, R. T. Rashid, X. Liu and Z. Mi, *Chem. Commun.*, 2019, **55**, 6305–6308.
22 K. Maeda, D. Lu, K. Teramura and K. Domen, *Energy Environ. Sci.*, 2010, **3**, 471–478.
23 K. Maeda, N. Sakamoto, T. Ikeda, H. Ohtsuka, A. Xiong, D. Lu, M. Kanehara, T. Teranishi and K. Domen, *Chem. – Eur. J.*, 2010, **16**, 7750–7759.
24 K. Maeda, D. Lu, K. Teramura and K. Domen, *J. Mater. Chem.*, 2008, **18**, 3539.
25 H. Huang, J. Feng, S. Zhang, H. Zhang, X. Wang, T. Yu, C. Chen, Z. Yi, J. Ye, Z. Li and Z. Zou, *Appl. Catal., B*, 2020, **272**, 118980.
26 M. Yoshida, K. Takanabe, K. Maeda, A. Ishikawa, J. Kubota, Y. Sakata, Y. Ikezawa and K. Domen, *J. Phys. Chem. C*, 2009, **113**, 10151–10157.
27 Y.-J. Cho, G. Moon, T. Kanazawa, K. Maeda and W. Choi, *Chem. Commun.*, 2016, **52**, 9636–9639.
28 A. Yamakata, M. Kawaguchi, N. Nishimura, T. Minegishi, J. Kubota and K. Domen, *J. Phys. Chem. C*, 2014, **118**, 23897–23906.
29 J. Tang, J. R. Durrant and D. R. Klug, *J. Am. Chem. Soc.*, 2008, **130**, 13885–13891.
30 K. Murofushi, K. Ogawa, H. Suzuki, R. Sakamoto, O. Tomita, K. Kato, A. Yamakata, A. Saeki and R. Abe, *J. Mater. Chem. A*, 2021, **9**, 11718–11725.
31 D. W. Bahnemann, M. Hilgendorff and R. Memming, *J. Phys. Chem. B*, 1997, **101**, 4265–4275.
32 T. Yoshihara, R. Katoh, A. Furube, Y. Tamaki, M. Murai, K. Hara, S. Murata, H. Arakawa and M. Tachiya, *J. Phys. Chem. B*, 2004, **108**, 3817–3823.
33 Y. Tamaki, A. Furube, M. Murai, K. Hara, R. Katoh and M. Tachiya, *J. Am. Chem. Soc.*, 2006, **128**, 416–417.
34 M. Barroso, C. A. Mesa, S. R. Pendlebury, A. J. Cowan, T. Hisatomi, K. Sivula, M. Grätzel, D. R. Klug and J. R. Durrant, *Proc. Natl. Acad. Sci. U. S. A.*, 2012, **109**, 15640–15645.
35 J. I. Pankove, *Optical Processes in Semiconductors*, Dover Publication, New York, 1975.
36 P. K. Basu, *Theory of Optical Processes in Semiconductors*, Oxford University Press, New York, 1997.
37 K. Wang, S. Olthof, W. S. Subhani, X. Jiang, Y. Cao, L. Duan, H. Wang, M. Du and S. (Frank) Liu, *Nano Energy*, 2020, **68**, 104289.
38 S. Zheng, W. Li, T. Su, F. Xie, J. Chen, Z. Yang, Y. Zhang, S. Liu, M. P. Aldred, K. Y. Wong, J. Xu and Z. Chi, *Sol. RRL*, 2018, **2**, 1700245.
39 J. Dong, J. Wu, J. Jia, X. He, Z. Lan, L. Fan, J. Lin and M. Huang, *ChemSusChem*, 2018, **11**, 619–628.
40 Y. Wang, K. Lopata, S. A. Chambers, N. Govind and P. V. Sushko, *J. Phys. Chem. C*, 2013, **117**, 25504–25512.
41 E. Arca, A. B. Kehoe, T. D. Veal, A. Shmeliov, D. O. Scanlon, C. Downing, D. Daly, D. Mullarkey, I. V. Shvets, V. Nicolosi and G. W. Watson, *J. Mater. Chem. C*, 2017, **5**, 12610–12618.
42 S. Ohkoshi, K. Nakagawa, K. Tomono, K. Imoto, Y. Tsunobuchi and H. Tokoro, *J. Am. Chem. Soc.*, 2010, **132**, 6620–6621.
43 L. Lin, Z. Lin, J. Zhang, X. Cai, W. Lin, Z. Yu and X. Wang, *Nat. Catal.*, 2020, **3**, 649–655.